

CHANDRA OBSERVATION OF A2256 — A CLUSTER AT THE EARLY STAGE OF MERGING

M. Sun, S. S. Murray, M. Markevitch & A. Vikhlinin¹

Harvard-Smithsonian Center for Astrophysics, 60 Garden St., Cambridge, MA 02138;
msun@cfa.harvard.edu

ABSTRACT

We present *Chandra* observations of the rich cluster of galaxies A2256. In addition to the known cool subcluster, a new structure (we call it "shoulder" in this paper based on its morphology) was resolved 2' east of the peak of the main cluster. It is shown as a localized feature embedded in the main cluster. Its position is roughly at the center of a low-brightness radio relic. Spectral analysis shows that the "shoulder" has high iron abundance ~ 1 (after the decomposition). The gas mass within it is around $2 \times 10^{11} M_{\odot}$. We suggest that this structure is either another merging component or an internal structure of the main cluster. The previously known subcluster has a low temperature (~ 4.5 keV) and high iron abundance (~ 0.6) in the central 150 kpc. The main cluster has the temperature of 7 - 8 keV and the iron abundance of 0.2 - 0.3 around the center. The *Chandra* image shows a relatively sharp brightness gradient at the south of the subcluster peak running south-south-east (SSE). A temperature jump was found across the edge, with lower temperature inside the subcluster. This phenomenon is qualitatively similar to the "cold fronts" found in A2142 and A3667. While a simple interpretation is not possible due to the projection, the edge indicates relative motion and contact of the two gas clouds. The *Chandra* temperature map shows only moderate temperature variations across the cluster, but not as strong as those expected in a major merger. If the "shoulder" is ignored, the temperature map resembles those simulations at the early stage of merging while the subcluster approached the main cluster from somewhere west. The observed temperature map and the edge-like feature near the south of the subcluster, imply that the ongoing merger is still at the early stage. The X-ray redshifts of several regions were measured. The results are consistent with a single value and all agree with the optical value. At least three member galaxies, including a radio

¹Also Space Research Institute, Moscow, Russia

head-tail galaxy, were found to have corresponding X-ray emission with X-ray luminosity from several times 10^{40} to 10^{41} ergs s $^{-1}$. It is found that the observed characteristics (temperature and iron abundance gradient) of the subcluster are similar to those of some poor clusters. The absence of galaxies around the peak of the subcluster is proposed to be the result of different falling velocity of the galaxies and the core gas.

Subject headings: galaxies: clusters: general — galaxies: clusters: individual (A2256) — merger — X-rays: galaxies

1. Introduction

In the hierarchical scenarios of the structure formation of the universe, cluster of galaxies are formed through subcluster mergers. Both observations (e.g. Bliton et al. 1998; Owen et al. 1999; Markevitch et al. 2000) and simulations (e.g. Roettiger, Loken & Burns 1997; Roettiger, Stone & Burns 1999; Bekki 1999) show that the merging dramatically change the physical characteristics of the intracluster medium (ICM) and galaxies, like the temperature, density and magnetic field strength of ICM, star formation rate and radio emission of galaxies. However, many processes related to the mergers and their effects are still vague. Hence systematic analyses of merging clusters are very helpful to deepen our understanding on this complex dynamical process. Here we present recent *Chandra* observations and analysis on the well-known merging cluster A2256.

A2256 is a rich cluster with strong X-ray emission ($L_x \sim 10^{45}$ ergs s $^{-1}$) at the redshift 0.058. *ROSAT* observations (Briel et al. 1991) clearly revealed two peaks near the center, separated by about 3.5'. One of them is roughly at the geometric center of the cluster, while the other one is considered to be a merging subcluster. The previous X-ray observations also showed that the subcluster has a lower temperature than the main cluster (Briel et al. 1991; Miyaji et al. 1993; Markevitch 1996, M96 hereafter) and temperature generally decreases with the radius (M96; Molendi, De Grandi & Fusco-Femiano 2000, MDF00 hereafter). Briel & Henry (1994) reported two hot spots (> 12 keV) in this cluster using *ROSAT* data. However, they were not confirmed by *ASCA* and *BeppoSAX* observations (M96; MDF00). The velocity dispersion of the galaxies is very large (~ 1300 km/s; Fabricant, Kent & Kurtz 1989) and the velocity distribution shows substructure (Roettiger, Burns & Pinkney 1995). The radio properties of A2256 are anomalous (Bridle & Fomalont 1976; Bridle et al. 1979; Röttgering et al. 1994, R94 hereafter). A remarkable radio relic, with sharp edges and possible filamentary structure, was found northwest of the two X-ray peaks. At least four head-tail sources were found, including one with an exceptional narrow, straight tail extending to at

least about 0.7 Mpc. R94 suggested that the halo was composed of a few head-tail galaxies that were heavily distorted due to the infalling subcluster. Recent *BeppoSAX* observation (Fusco-Femiano et al. 2000) also showed the existence of nonthermal X-ray emission from the cluster but only significant above 10 keV.

In this paper, we present the analysis of the recent *Chandra* observations of A2256. *Chandra* observations and data reduction are in §2. The analysis is in §3. §4 is the discussion and §5 is the summary. Throughout this paper, we assume $H_0 = 70 \text{ km s}^{-1} \text{ Mpc}^{-1}$ and $q_0 = 0.5$. These cosmological parameters correspond to the linear scale of 1.08 kpc/arcsec at the cluster redshift.

2. Observations and data reduction

A2256 was observed by *Chandra* three times with Advanced CCD Imaging Spectrometer (ACIS). The information of the observations are listed in Table 1. For each observation, we excluded the known bad columns, hot pixels, chip node boundaries and events with *ASCA* grades 1, 5 and 7, as well as bad aspect intervals. The proper gain map file for that period was used. Particle background flare periods were excluded based on the X-ray light curves from the outer parts of the field. The back-illuminated (BI) chips and front-illuminated (FI) chips were filtered separately since they have different background flare levels (see Markevitch et al. 2000 for details). The chips used for data analysis are I0 - I3 chips of the ACIS-I observation and S2 - S4 chips of the ACIS-S observation. The streak events in S4 chip were removed by the "destreak" tool in CIAO. The short observation 1521 was dominated by background flares (over 80% of its exposure time) and the statistics are quite poor so we do not include that data in our analysis.

To subtract the correct background, the blank field background dataset relevant for the period of the observations was used (Markevitch 2001). Since the background may change slightly with time, we also checked the background rate using the data at high energy (10-12 keV in the front-illuminated - FI chips and 9-12 keV in the back-illuminated - BI chips). It was found that the background normalization should be increased by 8% in FI chips, consistent with the expected long-term background trend. Note that although the correction should apply only to the particle component of the total background (and not the cosmic x-ray background or CXB), that component is dominant at energy greater than 2 - 3 keV which is most important for the gas temperature fitting. Small rescaling of the CXB component generally has only tiny effect on the spectral fitting. Thus we apply this correction across the energy range for simplicity. The systematic uncertainty of the background normalization ($\pm 10\%$) that encompasses this correction was also included in all the confidence intervals

reported below.

Shortly after the launch of *Chandra*, the ACIS FI chips suffered increasing "charge transfer inefficiency" (CTI) problem. The effect is seen as a decreasing quantum efficiency (QE) with increasing distance from the readout node. Here the results of the calibration observations of G21.5-0.9 were adopted to make CTI corrections (Vikhlinin 2000). We also used an additional position-independent correction factor of 0.93 for the ACIS-I quantum efficiency below 1.8 keV to account for the difference between ACIS-S3 and ACIS-I (Vikhlinin 2000). For hot clusters, ignoring it results in spuriously high temperature and the dependence of fitting results on the adopted low energy cut (Markevitch & Vikhlinin 2001). CIAO(1.1.5), FTOOLS(5.0), XSPEC(10.0) and some our own software were used to do the data reduction. The exposure maps were generated using our own software (equivalent to the similar one in CIAO). Since vignetting is dependent on the energy, narrow bands were used and weighting spectra were also applied in producing the exposure maps (the weighting spectra differ from chip to chip based on the fitting result of the integrated spectrum of each chip). To produce response files of the spectra in the interested regions (response matrices - RMF and auxiliary response files - ARF), the tools calcrmf and calcarf by Vikhlinin were used. The ARF was calculated by weighting the mirror effective area in the region with the observed cluster brightness distribution in 0.5 - 2.0 keV band. The RMF was calculated by weighting the standard set of matrices within the region by the observed cluster brightness distribution. All the errors in this paper are 90% confidence interval.

3. Analysis

3.1. Point sources

Over 30 point sources were detected in two observations using the CIAO wavelet detection tool. A detailed analysis on those point sources is beyond the scope of the paper. In this section, we will mainly discuss the point sources coincident with the member galaxies. Three member galaxies (all ellipticals) were found to have corresponding X-ray sources in both observations. They are shown in Fig. 1. One is the elliptical galaxy E (Fig. 2) which is also a radio head-tail galaxy (A in R94). Only about 50 counts from it in total were collected during the two observations. The statistics of the data do not allow us to constrain the temperature or the photon index well even if its spectrum is that simple. If we simply assumed a 1 keV thermal plasma with normal solar abundance, the derived luminosity is about 8×10^{40} ergs s $^{-1}$ (0.5 - 10 keV). If a powerlaw with photon index 1.7 is assumed, the derived luminosity is about 3×10^{41} ergs s $^{-1}$ (0.5 - 10 keV). The other two sources correspond to the NW core of the double galaxy NGC 6331 (C) and galaxy D respectively (Fig.

2). Only about 20 counts in total were collected from each source in the two observations. Their luminosity are estimated to be around 3×10^{40} ergs s $^{-1}$ for the 1 keV thermal plasma assumption, or 10^{41} ergs s $^{-1}$ for the powerlaw (photon index 1.7) assumption (0.5 - 10 keV). The X-ray emission may come from the low luminosity active galactic nuclei (LLAGN) or thermal halos.

We also tried to explore the nature of the brightest two point sources in the field (Fig. 1; #1: 7.5 c/ks - I3; #2: 5.4 c/ks - I0 and 8.4 c/ks - S3). #1 is also marginally seen in both *ROSAT* PSPC and HRI images. #1 has a very faint optical counterpart in DSS II while #2 has no counterpart. We extracted and fitted their spectra with a simple powerlaw model. If the absorption is fixed at the galactic value, the photon index for #1 and #2 are $1.4^{+0.5}_{-0.4}$ and 1.3 ± 0.4 respectively. Thus, they might be background AGNs. Based on these best-fit, their 0.5 - 10 keV unabsorbed flux are 10^{-13} ergs s $^{-1}$ cm $^{-2}$ and 7×10^{-14} ergs s $^{-1}$ cm $^{-2}$ respectively.

We also compared the observed source number with the predicted by the Log N - Log S relation derived in *Chandra* deep fields (e.g. Giacconi et al. 2001) and found no significant difference.

3.2. Structure of diffuse emission

The 0.5 - 7 keV combined ACIS-I/S image is shown in Fig. 1 overlaid on a DSS II image. The background was subtracted and the image was divided by the exposure map. All the point sources were excluded. The two previously resolved peaks at the center (P₁ and P₂ hereafter) by *ROSAT* (Briel et al. 1991) are prominent and both show internal structures (Fig. 2). It is noticed that the central part of the subcluster (the western peak) is elongated along the east-west direction, while the central part of the main cluster (the eastern peak) is elongated along the north-south direction (Fig. 1 and 2). These two peaks are separated by about 3' and P₂ is somewhat brighter. In DSS II image, there is no galaxy concentration around P₂. Radio head-tail galaxies E, F and G (Fig. 2) and double galaxy NGC 6331 (C) all have offsets to P₂ from 1' to 2'. The surface brightness peak of the main cluster is located 0.5' north of a big elliptical galaxy (B), while galaxy A, the galaxy with the most extended optical halo in A2256, is about 50 kpc east of the peak. Besides P₁ and P₂, a new structure was found significantly to the east of P₁ in *Chandra* observations (Fig. 1 and 2). In this paper we call it P₃ or "shoulder" from its morphology. This structure is shown as a small clump extended from P₁ but with a clear local maximum and seems to be embedded in the main cluster. The *ROSAT* images were re-checked and this structure was also found in both HRI and PSPC images though it is not very significant. It was also detected in the wavelet

analysis on PSPC data by Slezak, Durret & Gerbal (1994). This structure has interesting spectral characteristics and will be discussed later.

We also zoom-in the central part of A2256 to see any substructures around the center (Fig. 2). The wavelet decomposition tool (Vikhlinin, Forman & Jones 1997) was applied to the image and the reconstructed image (the right one in Fig. 2) is quite similar to the simply smoothed one (the left one in Fig. 2). Both images show complex structures around the center. P_1 and P_2 also show internal structures, which may also be a support for some kind of ongoing dynamical process in this cluster. However, the current data do not allow us to constrain the spectral difference on such small scales. Besides the "shoulder" and the substructures within P_1 and P_2 , there are still several interesting significant facts. First, there are no X-ray enhancements around the central biggest ellipticals A, B and C (the 3σ upper limits are all about 2×10^{41} ergs s^{-1} at 0.5 - 10 keV, assuming 1 keV thermal spectrum and 0.5' aperture size.). Second, the surface brightness gradient at the south of P_2 is sharper than those in other directions (more prominent in the unsmoothed image; also pointed out by Briel & Henry, 1991). Third, there is a protrusion which extends from the center of P_2 to the southwest. As shown in Fig. 6, after removing the main cluster, the southern parts become even sharper. In §3.6, we will show that it may be something like a cold front.

3.3. Temperature map

In view of the complex central structure mentioned in §3.2 and the fact that A2256 is very likely a cluster in merging, the knowledge of the temperature distribution can reveal us the nature of the structures and the merging. The resolution of the temperature map one can achieve for A2256 with *Chandra* is limited by statistics and the PSF effect can be ignored completely. We used the following method to obtain the temperature map. First, the field was divided into 30 regions (as shown in Fig. 3) with similar number of counts, then for each region we fitted the spectrum to get the temperature (for region # 11 - 30, we fitted the spectra from two observations simultaneously). In view of the uncertainty of the ACIS low energy response, only 0.9-9 keV data were used and the absorption was fixed to the galactic value 4.1×10^{20} cm $^{-2}$. The best-fit temperatures are not sensitive to any small excess in absorption. The redshift was fixed at 0.058 and the abundance was fixed at 0.3 solar (we used the solar abundance table by Anders & Grevesse 1989), which is the average value of previous observations (e.g. M96; MDF00). The MEKAL code in XSPEC was used. Second, we shifted the regions half-size along the parallel and perpendicular directions to the orientation of the first set of regions to get two additional similar temperature maps. The final one was obtained by averaging the above three. Then the final temperature map

was adaptively smoothed a little bit for a better presentation (Fig. 3). Two checks were performed. The first is the integrated temperature of the central 8.3' square (ACIS-S3 chip FOV, see Fig. 4). The result is $6.7^{+0.2}_{-0.2}$ keV, consistent with the central temperature (~ 7 keV) reported by previous observations (e.g. Miyaji et al. 1993; Markevitch & Vikhlinin 1997b; White 2000; MDF00). The second is that we did spectral fits at the same regions as those in *BeppoSAX* paper (MDF00). Our results generally agree with theirs within 0.5 keV, except in their region 2NW, where *BeppoSAX* spectrum may suffer the contamination from the nearby high temperature regions due to the large point spread function (PSF) of *BeppoSAX* (105" HPD for MECS at 1.5 keV).

On the 5 arcmin scale, the ACIS temperature map is in agreement with that of *ASCA* (M96). It shows moderate temperature variations across the cluster but not as strong as expected in a major merger (e.g. Roettiger et al. 1997 and other simulations). Combining this temperature map with the image, no shock was found in the field (a feature that is likely a "cold front" will be discussed in §3.6). The subcluster has lower temperature (~ 4 keV at the coolest region) than the main cluster and the shape of the low temperature regions strongly suggests that the subcluster entered the main cluster from somewhere west. This temperature map, if we omit the "shoulder", resembles those at the early stages of merging in simulations (e.g. Roettiger et al. 1997; Takizawa 1999; Takizawa 2000). It is also interesting that the apparent coolest part of the subcluster is about 2' west of its surface brightness peak. The main cluster appears largely undisturbed, as concluded by Markevitch & Vikhlinin (1997a) from the *ASCA* results. The central region of the main cluster is generally cooler than its outskirts covered by our FOV. This is more likely due to the projection of the cooler subcluster and possibly the "shoulder", rather than the genuine temperature gradient. There is a hot region (~ 9 keV; around regions #5 and #16 in Fig. 3) at the north of the main cluster. We notice that it is just in positional coincidence with the eastern lobe of the radio relic (Fig. 1). This might imply some kind of physical relation between the merging events and the radio relics. It is also noticed that there is a hot region near the south edge of the subcluster. In §3.6, we will show it might be related to a cold front. The two hot spots reported by Briel & Henry (1994) are located in the FOV of ACIS-I (Fig. 3). Our measurements ($7.9^{+1.3}_{-1.0}$ keV for their NE spot and $5.8^{+1.5}_{-1.2}$ keV for the SW one) do not confirm the existence of these hot spots, consistently with the earlier *ASCA* and *BeppoSAX* conclusions (Markevitch & Vikhlinin 1997a; MDF00).

We also checked the existence of any nonthermal component in the spectra, especially at the regions of the radio relic. No clear evidence for such component in ACIS spectra was found. A simple cooling flow component was also added to the spectral model but that never changed χ^2 significantly and the obtained mass accretion rates were always very small.

3.4. Iron abundance & red shift

The integrated abundance for the central $8.3'$ square (ACIS-S3 chip FOV) was obtained by simultaneously fitting the spectra of two observations. It is $0.34^{+0.06}_{-0.05}$, which is a little higher than the previous results for the whole cluster, 0.27 ± 0.06 by M96 (we converted their value for the abundance table used here) and 0.25 ± 0.03 by MDF00 (we converted their 68% confidence error into 90%). This is consistent well with the recent finding that the abundance generally falls with radius (MDF00) and their results in the inner radial bins. Here we are more interested in the distribution of iron. The statistics of the data do not permit a detailed analysis for the whole field. However, in checking spectra from the regions that we used for the temperature map, at least two with significantly high iron abundance areas were found. The results are shown in Fig. 4. The four solid line regions, from a to d, represent P_1 , P_2 , P_3 and a southern part of the main cluster (relatively far from the subcluster) respectively. The results from ACIS-I and ACIS-S agree well, so we performed simultaneous fits for each region. As shown in the figure 4, it is clear that P_2 and P_3 have more iron than P_1 and the southern main cluster region. The joint abundance-temperature 90% confidence regions for a - d are shown in Fig. 5, which again reinforces that a and d are different from b and c. Markevitch & Vikhlinin (1997b) also obtained a higher iron abundance at the subcluster than that of the main cluster using *ASCA* data but the difference was not significant, which may due to the wide PSF of *ASCA*. If we further consider the possible contamination of emission among the three structures due to projection, even higher abundance contrasts would be expected. The iron abundance in other regions (e.g. the outer parts of the subcluster and the north part of the main cluster) are all around the average (~ 0.3) but poorly constrained. Current data can not allow us to determine whether the high iron abundance is only localized in the "shoulder" or also present in its immediate surrounding. No iron abundance enhancement was found to be around galaxies C and E.

We also measured the redshifts in several regions from the iron $K\alpha$ line blend. The regions we chose among those in Fig. 4 are b (the subcluster), c (the "shoulder"), and the ACIS-S3 FOV excluding b, c and their $1'$ surrounding (the main cluster). The results are $0.056^{+0.008}_{-0.007}$, $0.064^{+0.007}_{-0.011}$, and 0.064 ± 0.010 respectively. All the values are consistent with a single redshift, suggesting that the main cluster, the subcluster and the "shoulder" are possible to be associated. Using the $\log N - \log S$ relation for clusters (e.g. Kitayama, Sasaki & Suto 1998; De Grandi et al. 1999), and considering the observed maximal difference of redshifts (~ 0.03), the possibility that they are a chance superposition is less than 10^{-4} . Therefore we conclude that they are very likely to be associated and interacting as also suggested by the temperature map and the possible cold front (§3.6).

The current data and calibration status do not allow us to constrain the spatial dis-

tribution of other elements, like silicon. The integrated silicon abundance in the ACIS-S3 FOV is 0.50 ± 0.23 while the *ASCA* result is 0.97 ± 0.39 for the whole cluster (Fukazawa et al. 1998).

3.5. Decomposition of the structures

Chandra observations reveal complex structures around the center of A2256. We should realize that due to the projection the observed spectra, especially those around the center, have at least two components entangled — the main cluster and the subcluster. It would be very helpful for our understanding if we can separate them. However, this is actually very hard since the merging clusters are not in hydrostatic equilibrium and we do not yet know their relative geometry. Here, we just present a very simple way to isolate the subcluster and decompose the spectral components. Briefly speaking, we tried to use a β -model to represent the main cluster (not the whole cluster) and examine the residuals. Then we can use those information to separate the spectral components in observed spectra. The *ROSAT* image (background-subtracted and exposure-corrected) shows that the surface brightness is rather spherical in the outer parts, especially after we exclude the subcluster region using a circle with some radius ($\sim 7'$) centered at the core of the subcluster. Thus we can simply measure the surface brightness beyond that subcluster region to make a β -model fit to the main cluster.

The outer contours of the *ROSAT* PSPC images were used to find the geometric center of the main cluster, which is about $1'$ south of the apparent peak of the main cluster. It is shown in Fig. 6. Then a $7'$ radius circle centered at the peak of the subcluster was used to represent the subcluster and a $2'$ radius circle at P_3 was used to represent the emission from the "shoulder". Only radial surface-brightness measurement outside of these circles was made. All the point sources were excluded. ACIS-I/S and PSPC data were used. The derived core radius is 3.8 ± 0.3 arcmin (or 0.25 ± 0.02 Mpc), and β is 0.58 ± 0.04 . The residual after removing the best-fit β -model of the main cluster is shown in Fig. 6. The "shoulder" is more prominent and the morphology of the subcluster is distorted, which is natural for a falling cluster. Moreover, the southern surface brightness has become sharper and points SSE, appearing more edge-like.

Then we can try to disentangle the spectral components in the observed spectra. From the temperature map and the observed surface density discontinuity (§3.6), it is known that the subcluster enters the main cluster from the west. Thus we do not expect much projection effect from the subcluster on P_1 . Here we only want to investigate P_2 and P_3 (the two regions in Fig. 2). To do that, we first need to assume the temperature of the contaminating gas

from the main cluster at P_2 and P_3 . Three values, 7, 8 and 9 keV, were assumed. The abundance of the main cluster gas was fixed at 0.3. The normalization of the contaminating gas is obtained from the best-fit β -model. The results are shown in Table 2. As expected, we obtained larger contrasts on temperature and abundance between the main cluster and the others. The abundance of the "shoulder" is still high after the decomposition. From the best-fit emission measure, assuming a constant density sphere, its gas mass is around $2 \times 10^{11} M_{\odot}$ if its dimension along the line of sight is not very different from others.

3.6. The SSE edge — a moving cold front?

Fig. 6 shows a clear edge-like structure running along the SSE direction. We measured the surface brightness profile in the linear regions parallel to the edge in the co-added ACIS image (not the residual). The temperature at each side of the edge are also obtained in the regions shown in Fig. 6. The results are shown in Fig. 7. At the edge, there is a break in the surface brightness profile that indicates a density discontinuity and a temperature jump from about 4.5 keV to about 8.5 keV. This feature is quite similar to the cold fronts found in A2142 by Markevitch et al. (2000) and A3667 by Vikhlinin et al. (2001a). In A2142 and A3667, these features delineate the contact surfaces of the cold dense clouds and the surrounding hotter gas, through which they move. In the case of A2256, the geometry is more complicated and there is projection of multiple structures. Therefore, it is not possible to derive the real density and pressure contrast across the edge. The flat shape of the edge may imply that it is only part of the whole moving edge (the other parts are smoothed out by projection if the moving front is tilted from the plane of sky), or the moving front viewed by an angle with the line of sight. The protrusion mentioned in §3.2 might be related to the striping gas of the subcluster or its wake.

This discovery, adds another candidate to the list of merging clusters which have cold fronts — A2142, A3667 and RXJ1720.1+2638 (Mazzotta et al. 2001). More cold fronts could be expected when more *Chandra* data are available. Systematic studies of such phenomena will enrich our knowledge on merging of the clusters.

4. Discussion

4.1. The nature of the "shoulder"

Chandra observations reveal a new structure - the "shoulder" - near the center, a localized feature with size about 3' and gas mass about $2 \times 10^{11} M_{\odot}$ (assuming a constant density

sphere and its dimension along the line of sight is similar as others). Its spectrum implies that iron is enriched in this structure (~ 1 after the decomposition). Two galaxies (D and H in Fig. 2) are apparently located in this structure though they are not necessarily associated with it. Bridle & Fomalont (1976) found a $10'$ low-brightness radio relic roughly centered at galaxy D (also the radio source D in the same paper) besides the bright NW halo (Fig. 1). The "shoulder" is within that diffuse radio relic.

Although the roughly similar temperature and abundance between this structure and the center of the subcluster may suggest that it is a remaining of the subcluster spread along the path of its infall, its location (east of P_1) is inconsistent with the infalling direction (somewhere from the west) of the subcluster suggested by the temperature map, the possible cold front and the general direction of the radio head-tail sources (E, F and G in Fig. 2).

Since its X-ray redshift suggests it is a feature inside A2256 (§3.4), only two choices are left: either a new merging component or an internal structure of the main cluster. Another merging component seems to be a feasible explanation. In fact, if we ignore the subcluster, the *Chandra* image resembles simulated images for a merger between a massive cluster and a much less massive one at about 0.3 Gyr after core crossing (e.g. Takizawa 1999; Takizawa 2000). The fact that there are two big elliptical galaxies rather than one dominant galaxy around the center also supports the idea that the main cluster has not yet relaxed well. Hence, we suggest that A2256 may be a system with three clusters (or two clusters and one group) in merging. About 0.3 Gyr before the ongoing merger, there was a merger between the massive cluster and a less massive system. The less massive system might be a galaxy group that did not disturb the potential well of the massive cluster much. The "shoulder" might be the relic of its core and galaxy B might be once the dominant galaxy of that less massive system since it is 2 times less luminous than A. González-Casado, Mamon & Salvador-Solé (1994) found such kind of the relic of the core can survive in at least one cluster crossing. The observed iron abundance difference between the "shoulder" and P_1 might suggest it was an off-center merger. The less massive system may have fallen into the massive cluster somewhere from the west as implied by the simulations and the relatively sharper surface brightness at the east than other directions. Under such scenario, the low-brightness radio relic found by Bridle & Fomalont (1976) would be related to this earlier merger event and the much brighter NW one may be related to the ongoing merger. The fading of the radio haloes after the merger was discussed by Tribble (1993). The typical aging time-scale is at the order of 10^8 years, consistent with our picture here.

Another possibility is that the "shoulder" is an internal structure of the main cluster as the two local dips of the potential around the D galaxies in Coma (Vikhlinin et al. 2001b). The gas mass of the "shoulder" is about $2 \times 10^{11} M_\odot$, while cD galaxies in clusters of galaxies

often have gas content at the level of $10^{11} - 10^{12} M_{\odot}$ (Trimble 2000). The galaxy A, which resembles the cD most in A2256, is quite near the "shoulder". Before the ongoing merger, the galaxy A may be at the center of the "shoulder", which could be the halo of hot gas. When the ongoing merger began, the gases (the "shoulder") might lag behind the galaxy A similar to the case discussed in §4.2. The iron mass excess within it is estimated to be about $10^8 M_{\odot}$, while the stellar mass of A is estimated to be about $7 \times 10^{11} M_{\odot}$ assuming $M/L = 7(M/L)_{\odot}$ and $L_B = 10^{11} M_{\odot}$. Thus, an injection of iron about 0.03% of the stellar mass of A is needed to explain the iron excess, which is still possible in the galactic-wind models (e.g. Arimoto & Yoshii 1987).

4.2. The nature of the subcluster and the merger

Fabian & Daines (1991) suggested that the subcluster had a cooling flow based on *ROSAT* observations. In §3.5 it is shown that the real temperature of the subcluster is about 4.5 keV around the center. The estimated gas density at the central 80 kpc of the subcluster is about $3.6 \times 10^{-3} \text{ cm}^{-3}$ from the spectral fitting. The cooling time scale is 85 Gyr $(n/10^{-3} \text{ cm}^{-3})^{-1} (T/8.6 \text{ keV})^{1/2}$, where n and T are the density and temperature of the gas. Our revised cooling time at the center of the subcluster is 14 - 20 Gyr. Though the estimated cooling time cannot completely rule out the existence of the cooling flow, neither the image nor spectra require any present cooling flow around the center of the subcluster.

§3.5 shows that the central 150 kpc of the subcluster has high iron abundance (~ 0.6), which decreases to about 0.3 at the outer parts. Briel & Henry (1991) divided the galaxies in A2256 into two groups using a simultaneous fit of two Gaussians to the whole velocity data, though the two redshift distribution components are not spatially separated. Based on their fit, they suggested that the subcluster was a poor cluster. Indeed, the observed X-ray characteristics of this subcluster resemble those of some poor clusters (Virgo by Matsumoto et al. 1996; Centaurus by Fukazawa et al. 1994; AWM 7 by Xu et al. 1997 and Ezawa et al. 1997). All of them have comparably low (or lower) temperature with the subcluster in A2256 and similar abundance gradients. However, all these poor clusters have central cooling flows while as discussed above, currently there is no cooling flow in the subcluster. One possibility is that the cooling flow of the subcluster has been destroyed by the early interaction during the merger while the abundance gradient was kept.

It is interesting that there is no galaxy concentration near the surface brightness peak of the subcluster. A natural explanation would involve the different falling velocity of the galaxies (here they may be C, E, and F) and the gas. The gas may lag behind the galaxies due to the drag by the main cluster gas, which is implied by the highly distorted shape of the

subcluster gas and the apparent contact discontinuity. We investigate whether this picture is applicable to galaxy C, the best candidate of the cD of the subcluster according to its halo size. Though both galaxies and gas may undergo spiral-in, deceleration or acceleration, the time from when they began to separate could be simply expressed as $0.1 \text{ Mpc} \sin^{-1}\theta / (V_C - V_G)$, where θ is the angle with the line of sight, V_C and V_G are the velocity of the galaxy C and gas respectively. For a time scale of 0.5 Gyr, a velocity difference about $200 \sin^{-1}\theta \text{ km s}^{-1}$ can explain the observed displacement. Since large velocity dispersion ($\sim 1300 \text{ km s}^{-1}$) was found in this cluster, a velocity difference ($V_C - V_G$) around several hundred km s^{-1} is quite possible.

The temperature map and the observed surface density discontinuity imply that the subcluster entered the main cluster from somewhere west. However, current data do not allow us to make a definite conclusion to the moving direction of the subcluster. It has been suggested that mergers may amplify the magnetic field and be responsible for the strong radio haloes and relics (Tribble 1993; Roettiger et al. 1999). The NW bright radio relic in A2256 appears to be located near the moving path of the subcluster, thus it is likely associated with the ongoing merger event. Finally, the temperature map excludes any significant disturbance of the cluster, indicating that the merger with the subcluster is at very early stage.

5. Summary

Chandra observations of the merging cluster A2256 confirm some of our previous understanding on it, but also reveal some new phenomena. Our results are summarized below:

1) A new structure ("shoulder") was found $2'$ east of the peak of the main cluster. It is shown as an extension from the main cluster peak but with local maximum. Several galaxies (A, D and H in Fig. 2) are near or apparently within it, but the physical association is hard to be established. The position is also roughly at the center of a low-brightness radio relic. This feature is also characterized by a high iron abundance (~ 1 after decomposition). Its temperature is comparable to or somewhat lower than that of the surrounding. The gas mass within this structure is about $2 \times 10^{11} \text{ M}_\odot$. We suggest that it is either a relic of a prior merger or an internal structure of the main cluster.

2) The subcluster was found to have a higher abundance (~ 0.6), but a lower temperature (4.5 - 5 keV) than the main cluster (0.2 - 0.3 and ~ 7 keV respectively). Its characteristics resemble some of the poor clusters. The morphology of the subcluster is distorted, which could be due to the infall. The central part of the subcluster, as well as the main cluster, show some internal structures.

- 3) The brightness profile across the southern edge of the subcluster indicates a density discontinuity and the temperature jump from about 4.5 keV inside the dense gas to about 8.5 keV outside. This probably indicates a contact the subcluster and the main cluster gases and their relative motion, somewhat similar to A2142 and A3667 (Markevitch et al. 2000; Vikhlinin et al. 2001a), although the geometry is more complex. Due to the projection, the real moving direction of the whole edge is not easy to be determined and the jumps of density and pressure are hard to be constrained.
- 4) The temperature map shows moderate temperature variation across the cluster, but not as strong as expected in a major merger. The temperature map implies that the subcluster entered the main cluster from somewhere west and the merger is still at the early stage. The main cluster appears not yet largely disturbed by the merger with the subcluster. The two hot spots reported by Briel & Henry (1994) are not confirmed.
- 5) No X-ray enhancement is detected around the two brightest galaxies (A and B in Fig. 2; the 3σ upper limits are about 2×10^{41} ergs s $^{-1}$ at 0.5 - 10 keV) around the center of the main cluster. Over 30 point sources were detected in the observations, but only 1/3 of them have optical counterparts (usually faint) in the DSS II image. No significant excess of point sources was found in the field. Three member galaxies near the center, including a radio head-tail source and a dumbbell-like big elliptical, were found to have corresponding X-ray point-like emission. Their X-ray luminosity were estimated to be several times 10^{40} - 10^{41} ergs s $^{-1}$.

The results presented here are made possible by the successful effort of the entire *Chandra* team to build, launch, and operate the observatory. We are grateful to the referee for the valuable comments to improve the manuscript. We acknowledge helpful discussions with W. Forman, C. Jones, D. M. Neumann, T. Clarke and F. Durret. This study was supported by NASA contract NAS8-38248.

REFERENCES

Anders E., & Grevesse N. 1989, *Geochimica et Cosmochimica Acta*, 53, 197
Arimoto, N., & Yoshii, Y. 1987, *A&A*, 173, 23
Bekki, K. 1999, *ApJ*, 510, 15
Bliton, M., Rizza, E., Burns, J. O., Owen, F. N., & Ledlow, M. J. 1998, *MNRAS*, 301, 609
Bridle, A., & Fomalont, E. 1976, *A&A*, 52, 107

Bridle, A., Fomalont, E., Miley, G., & Valentijn, E. 1979, A&A, 80, 201

Briel, U. G. et al. 1991, A&A, 246, L10

Briel, U. G., & Henry, J. P. 1994, Nature, 372, 439

De Grandi, S., & Molendi, S. 1999, ApJ, 527, L25

Ezawa, H. et al. 1997, ApJ, 490, L33

Fabian, A. C., & Daines, S. J. 1991, MNRAS, 252, 17P

Fabricant, D. G., & Kent, S. M., & Kurtz, M. J. 1989, ApJ, 336, 77

Fukazawa, Y. et al. 1994, PASJ, 46, L55

Fukazawa, Y. et al. 1998, PASJ, 50, 187

Fusco-Femiano, R. et al. 2000, ApJ, 534, L7

Giacconi, R. et al. 2001, ApJ submitted (astro-ph/0103014)

González-Casado, G., Mamon, G. A., & Salvador-Solé, E. 1994, ApJ, 433, L61

Kitayama, T., Sasaki, S., & Suto, Y. 1998, PASJ, 50, 1

Markevitch, M. 1996, ApJ, 465, L1 (M96)

Markevitch, M., & Vikhlinin, A. 1997a, ApJ, 474, 84

Markevitch, M., & Vikhlinin, A. 1997b, ApJ, 491, 467

Markevitch, M. et al. 2000, ApJ, 541, 542

Markevitch, M. 2001, *Chandra* calibration memo, <http://asc.harvard.edu/cal/>, "ACIS", "ACIS background"

Markevitch, M., & Vikhlinin, A. 2001, ApJ, in press (astro-ph/0105093)

Matsumoto, H. et al. 1996, PASJ, 48, 201

Mazzotta, P., Markevitch, M., Vikhlinin, A., Forman, W. R., David, L. P., & Vanspeybroeck, L. 2001, ApJ, 555, 205

Miyaji et al. 1993, ApJ, 419, 66

Molendi, S., De Grandi, S., & Fusco-Femiano, R. 2000, ApJ, 533, L43 (MDF00)

Owen, F., N., Ledlow, M., J., Keel, W., C., & Morrison, G., E. 1999, AJ, 118, 633

Roettiger, K., Burns, J. O., & Pinkney, J. 1995, ApJ, 453, 634

Roettiger, K., Loken, C., & Burns, J. O. 1997, ApJS, 109, 307

Roettiger, K., Stone, J. M., & Burns, J. O. 1999, ApJ, 518, 594

Röttgering, H., Snellen, I., Miley, G., De Jong, J. P., Hanisch, R. J., & Perley, R. 1994, ApJ, 436, 654 (R94)

Slezak, E., Durret, F., & Gerbal, D. 1994, AJ, 108, 1996

Takizawa, M. 1999, ApJ, 520, 514

Takizawa, M. 2000, ApJ, 532, 183

Tribble, P. C. 1993, MNRAS, 263, 31

Trimble, V. 2000, in Allen’s Astrophysical Quantities, fourth edition, ed. A. N. Cox (Springer AIP press), p577

Vikhlinin, A., Forman, W., Jones, C. 1997, 474, L7

Vikhlinin, A. 2000, *Chandra* calibration memo, http://asc.harvard.edu/cal/Links/Acis/acis/Cal_prods/qe/

Vikhlinin, A., Markevitch, M., & Murray, S. S. 2001a, ApJ, 551, 160

Vikhlinin, A., Markevitch, M., Forman, W., & Jones, C. 2001b, ApJL, 555, 87

White, D. A. 2000, MNRAS, 312, 663

Xu, H. et al. 1997, PASJ, 49, 9

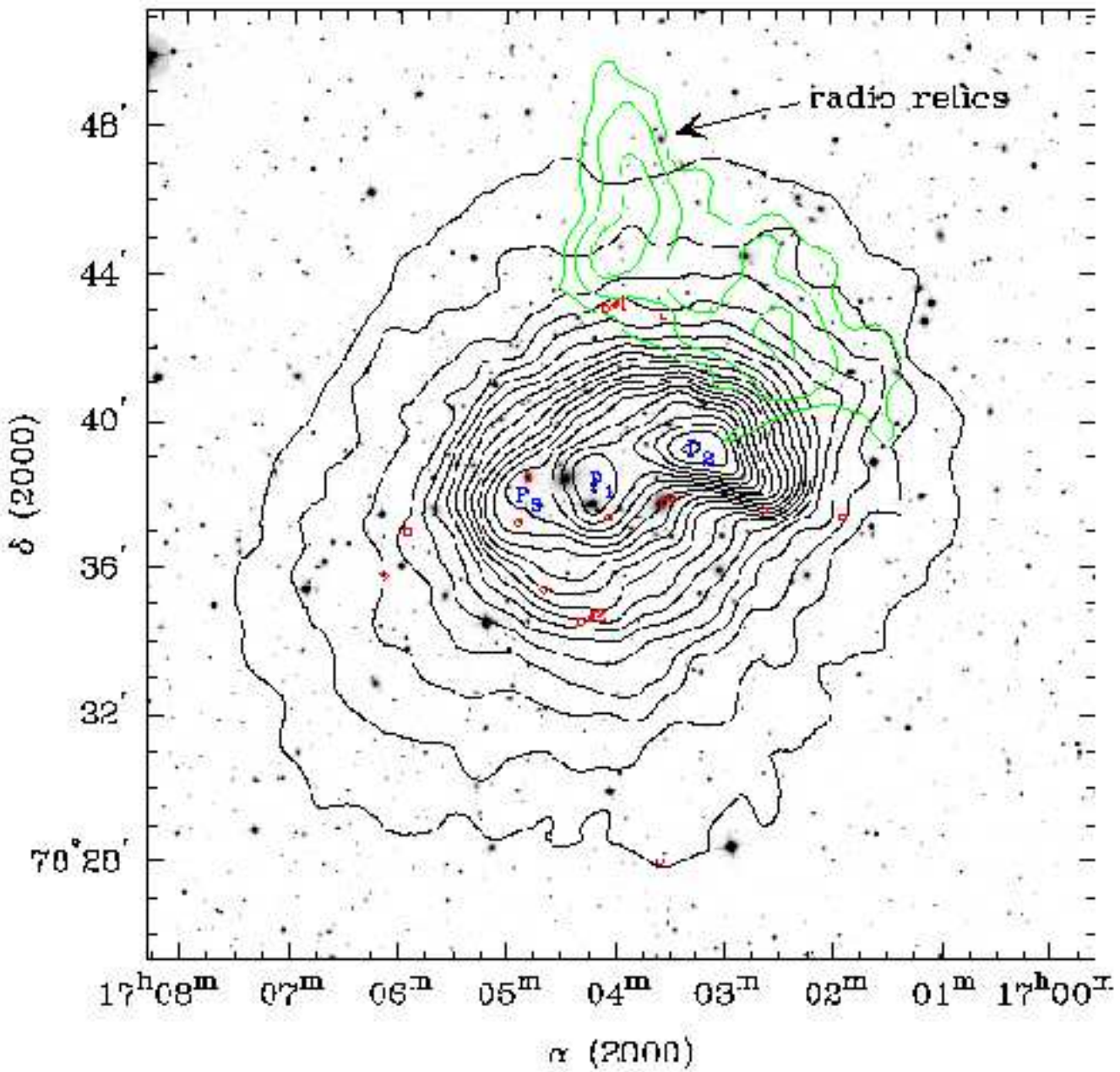


Fig. 1.— The 0.5 - 7 keV ACIS-I/S co-added contours (point sources excluded) overlaid on a Digitized Sky Survey second generation red (DSS II hereafter) image. The ACIS-I/S image was smoothed by a variable-width Gaussian whose σ varies from $20''$ at the peak to $30''$ near the edges of the image. The contour levels are linear from 0.03 to 0.625 c/ks/pixel (pixel size: $3.934''$). The outermost contour is affected by the edges of the CCD chips. P_1 , P_2 and P_3 correspond to the peak region of the main cluster, the peak region of the subcluster and the "shoulder" respectively. The small red circles represent the bright point sources (> 20 counts) detected by ACIS-I/S, including the three corresponding to member galaxies. #1 and #2 are the two brightest point sources (see §3.1). The green contours show the position of the strongest radio relic in this source (from NVSS 20 cm survey). There are more diffuse radio relics around P_2 and P_3 (Bridle & Fomalont 1976; R94).

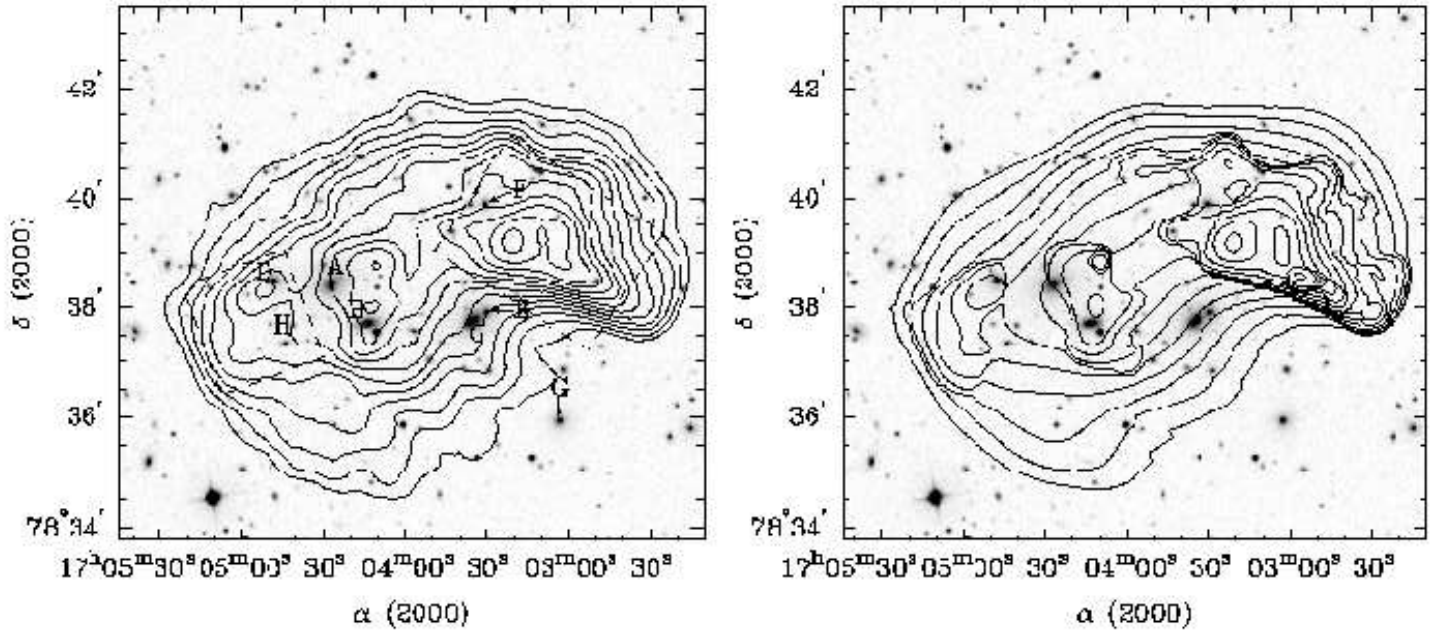


Fig. 2.— The left one: central region of the 0.5 - 7 keV ACIS-I/S co-added image (linear-spaced contours) overlaid on the DSS II image. The ACIS-I/S image was smoothed by a $15''\sigma$ Gaussian. We used A - H to label the big galaxies around the center. Their redshifts are 0.0594, 0.0564, 0.0586, 0.0643, 0.0587, 0.0586, 0.0553 and 0.0508 from A to H respectively (from NASA extragalactic database — NED). The arrows for E, F and G (all radio head-tail sources) show the rough directions of the head-tails. Notice the "shoulder" east of A, the southern "edge" of P_2 (see Fig. 1) and the SW protrusion from P_2 . The dash boxes represent the two substructures around the center and analysis was made to these regions in section §3.6. The right one: the reconstructed image (linear-spaced contours) by wavelet analysis in the same region as the left. This image also reveals the complicated structure at the center with very similar pattern as the left. The surface density discontinuity is enhanced in this wavelet reconstructed image.

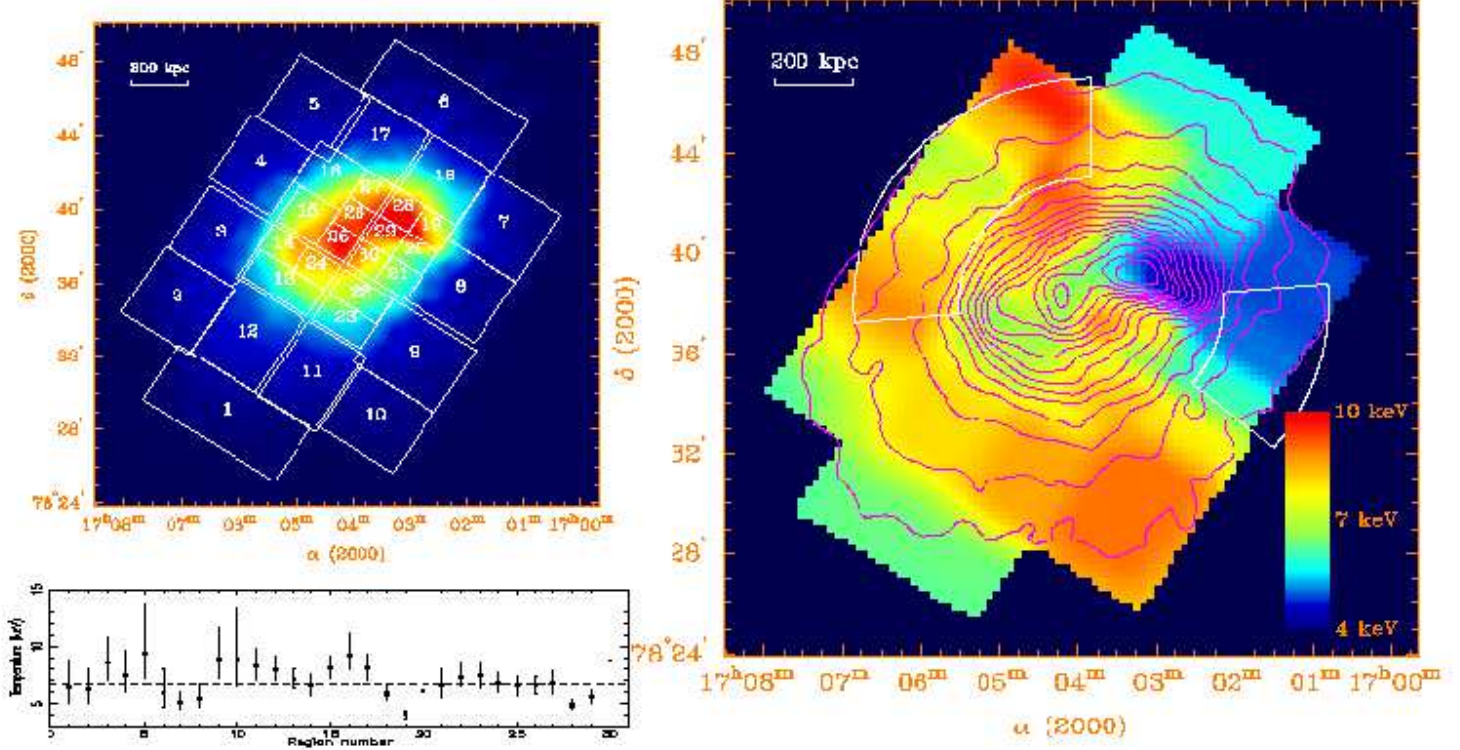


Fig. 3.— Temperature map. Upper left panel: the first set of regions we chose (the second and third sets are regions shifted high region size relative to the first set); Lower left panel: the fitting results for the first (of three) set of regions (The results for the second and third sets agree with those of the first set); the dash line represents the average temperature measured in the central 8.3' square ACIS-S3 FOV — 6.7 keV. Right panel: The adaptively smoothed image of the final temperature map. The average smoothing scale (σ) is 0.5'. This map is the average of the results of three overlapping sets of region described in the text, not simply the smoothing from the results shown on the left. The errors on this temperature map can be estimated from the lower left panel. Two sectors shown in white are the "hot spots" reported by Briel & Henry (1994).

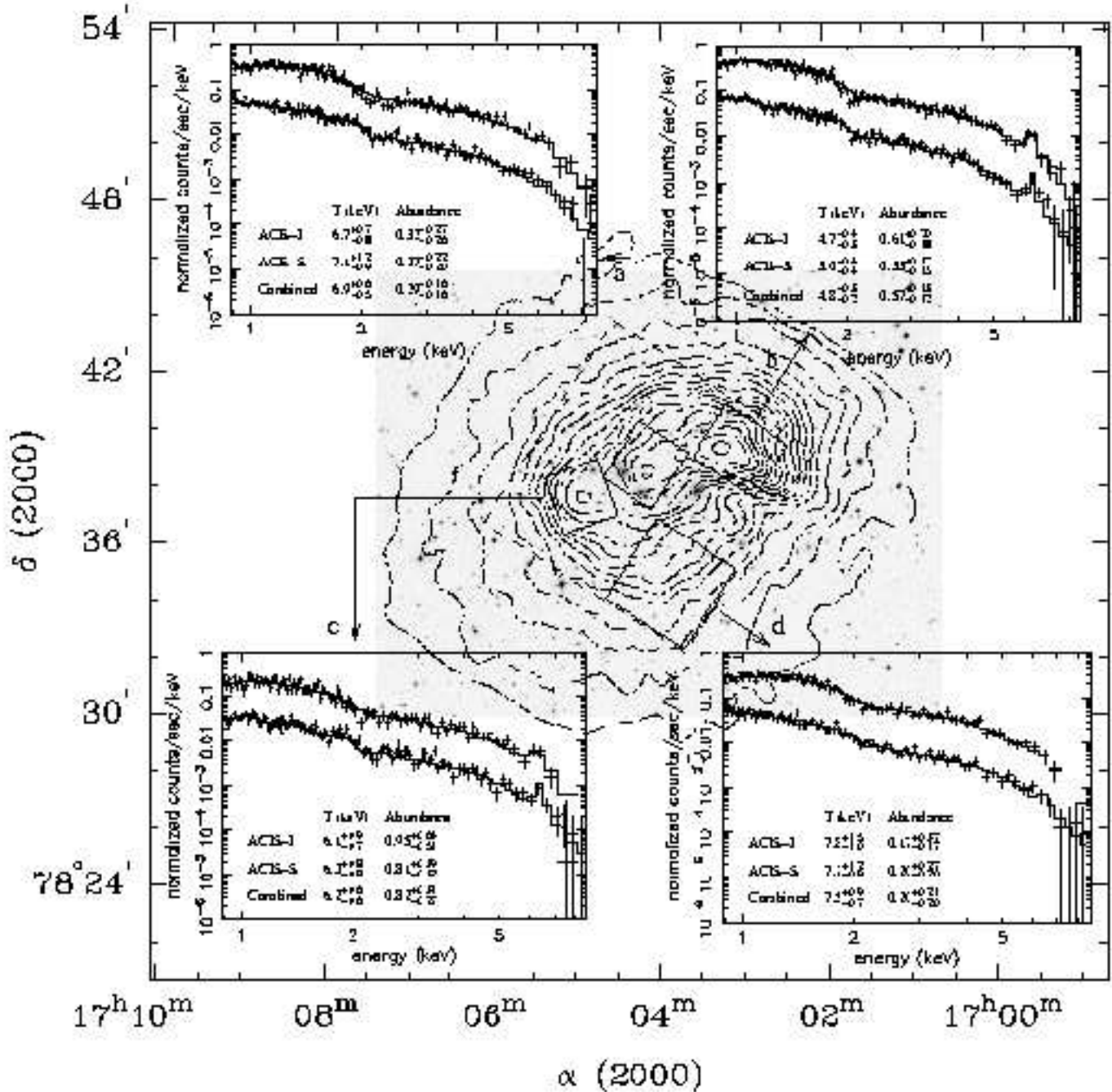


Fig. 4.— Iron abundance in several interesting regions: a - P_1 ; b - P_2 ; c - P_3 ; d - a southern region. Region c is same as what we used in Fig. 2 for P_3 . Regions a and b cover basically same regions as what we used in Fig. 2 for P_1 and P_2 but are not crossing the chips. In each small box, the upper spectrum is that of ACIS-I and the lower one is that of ACIS-S rescaled by 0.1. Both spectra and fitting results suggest that P_2 and P_3 have more iron than P_1 and the southern region d. The square dash region is the FOV of ACIS-S3 chip in observation 965. The contours are from ACIS-I observation 1386 and the gray image is DSS II.

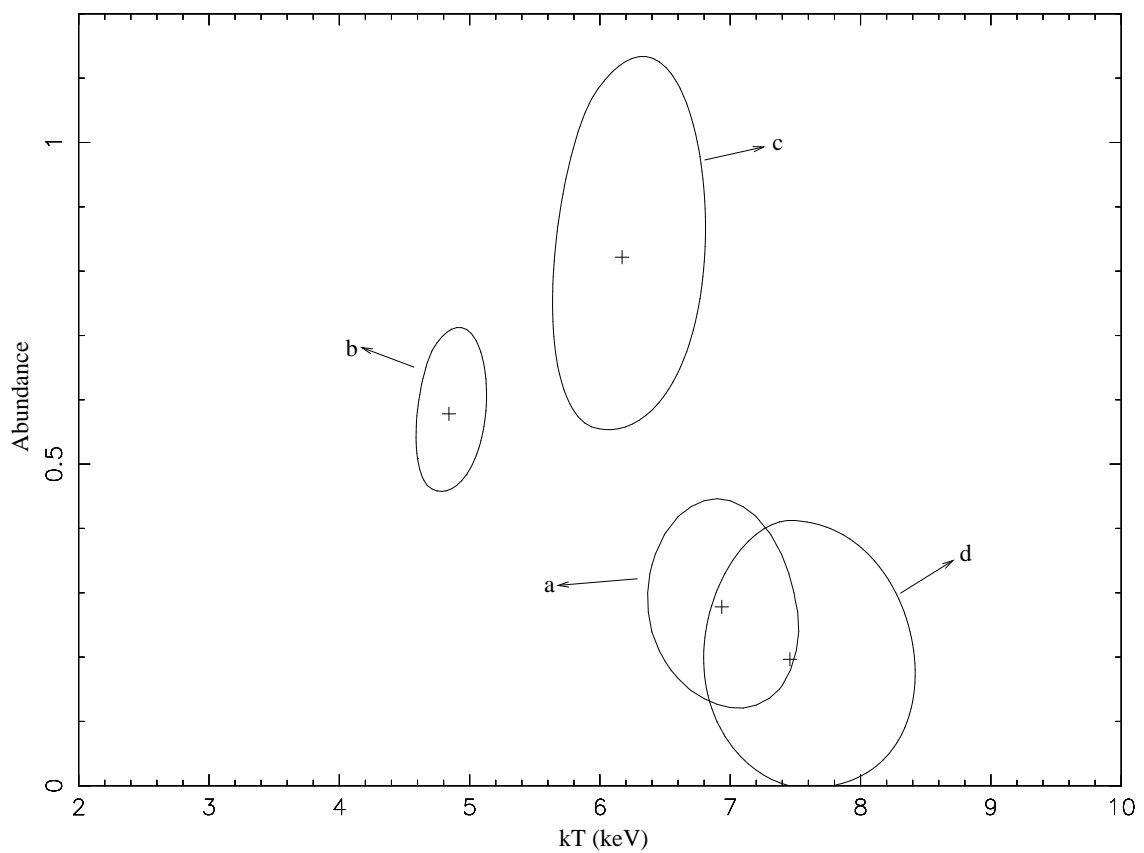


Fig. 5.— The joint abundance-temperature 90% confidence regions for four regions in Fig. 4.

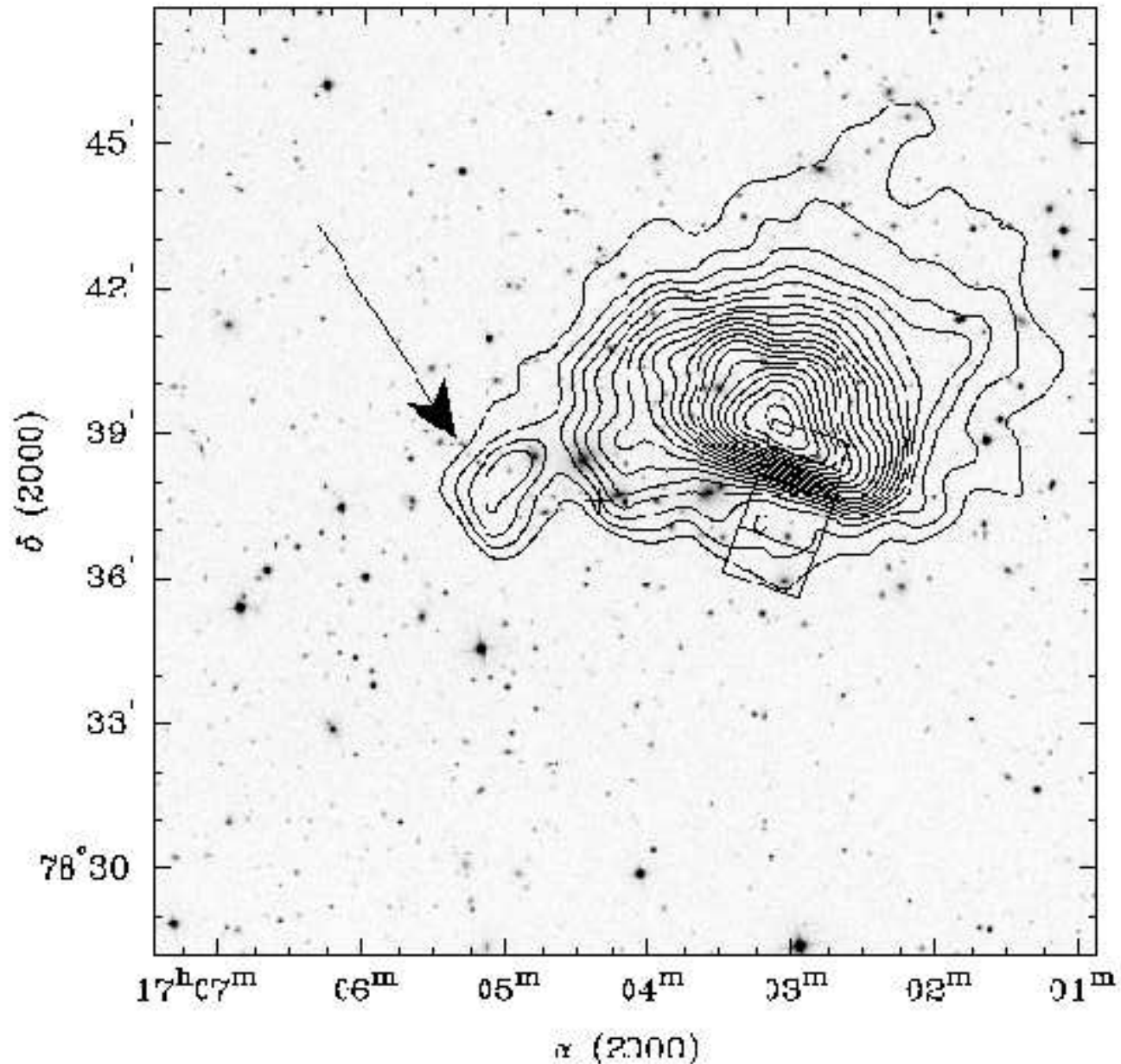


Fig. 6.— Residual after removing the main cluster represented by the best-fit β -model. The residual was smoothed by a variable-width Gaussian whose σ varies from $16''$ at the peak to $30''$ near the edges of the image. The contour levels are linearly from 0.03 to 0.98 of the maximum with an interval 0.05 of the maximum. The "shoulder" is very prominent — pointed by the arrow. The edge at the south of the subcluster peak is very clear. The four regions in line are those that we made temperature measurement in §3.6. The cross is the derived geometrical center of the main cluster.

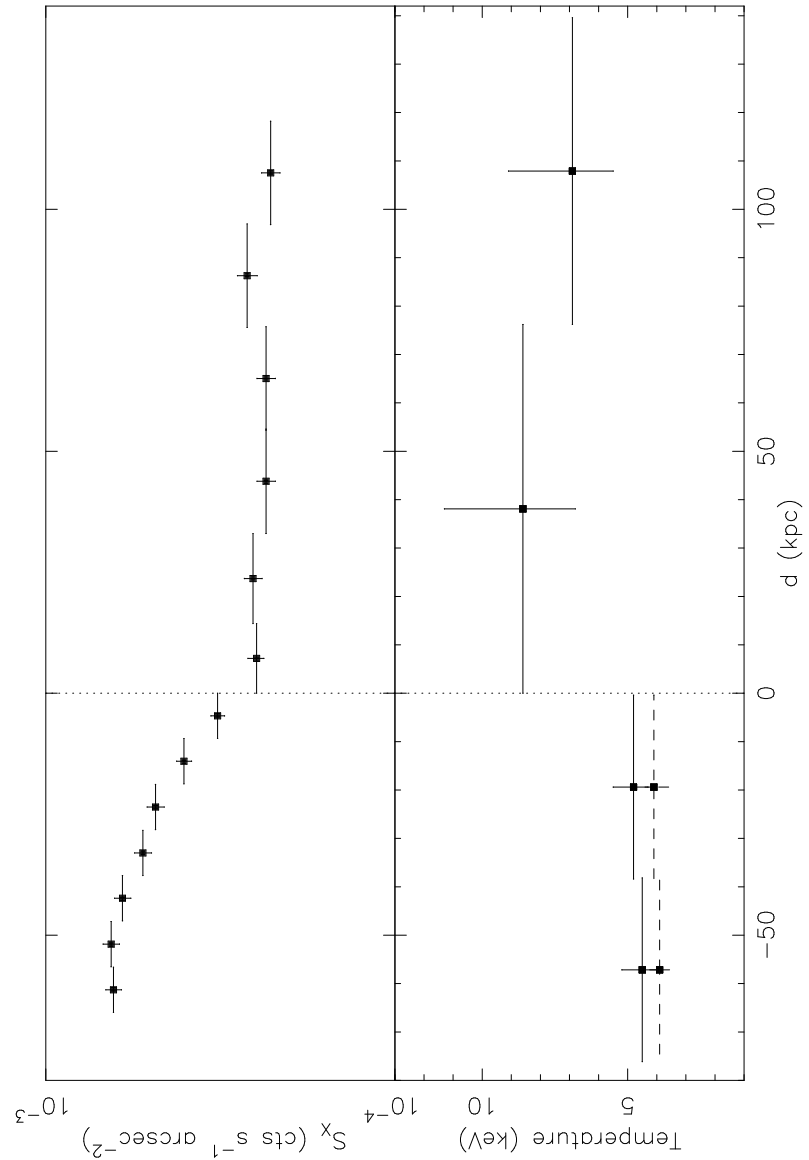


Fig. 7.— The projected surface brightness profile (measured in co-add ACIS-I/S image) and temperature across the edge. The regions are shown in Fig. 6. The distance is measured relative to the edge. The temperature fits represented by the dash lines are the decomposed temperature using the method mentioned in §3.5.

TABLE 1

OBSERVATIONS

Obs. ID	1386	965	1521
Obs. Mode	ACIS-I, 012378	ACIS-S, 236789	ACIS-S, 136789
Observing time	Oct. 13, 99	Oct. 13, 99	Feb. 27, 00
Total exposure (s)	15809	15717	2976
Effective exposure (s)	9966	8256(S3), 9458(S2,S4)	-
RA (2000)	17:04:14	17:04:36	17:04:22
DEC (2000)	78:37:52	78:36:18	78:39:59

TABLE 2

DECOMPOSITION OF P₂ AND P₃

Region	T ^a (keV)	Abund. ^a	T ^b (keV)	Abund. ^b	T ^c (keV)	Abund. ^c	T ^d (keV)	Abund. ^d
P ₂	5.0 ^{+0.3} _{-0.3}	0.51 ^{+0.12} _{-0.11}	4.3 ^{+0.3} _{-0.3}	0.59 ^{+0.17} _{-0.14}	4.2 ^{+0.3} _{-0.3}	0.56 ^{+0.16} _{-0.14}	4.0 ^{+0.3} _{-0.3}	0.55 ^{+0.17} _{-0.13}
P ₃	6.2 ^{+0.6} _{-0.6}	0.82 ^{+0.31} _{-0.27}	5.0 ^{+1.3} _{-1.1}	> 0.75	4.5 ^{+1.0} _{-1.0}	> 0.68	3.9 ^{+1.1} _{-0.8}	> 0.55

^a Uncorrected

^b After the decomposition (7 keV assumption, see text)

^c After the decomposition (8 keV assumption, see text)

^d After the decomposition (9 keV assumption, see text)